The Astrophysical Journal, 803:15 (13pp), 2015 April 10 doi:10.1088/0004-637X/803/1/15
© 2015. The American Astronomical Society. All rights reserved.

MULTI-WAVELENGTH OBSERVATIONS OF 3C 279 DURING THE EXTREMELY BRIGHT GAMMA-RAY FLARE IN 2014 MARCH–APRIL

Vaidehi S. Paliya[1,2], S. Sahayanathan[3], and C. S. Stalin[1]
[1] Indian Institute of Astrophysics, Block II, Koramangala, Bangalore-560034, India; vaidehi@iiap.res.in
[2] Department of Physics, University of Calicut, Malappuram-673635, India
[3] Astrophysical Sciences Division, Bhabha Atomic Research Centre, Mumbai-400085, India
Received 2014 December 19; accepted 2015 January 28; published 2015 April 7

ABSTRACT

The well-studied blazar 3C 279 underwent a giant γ-ray outburst in 2014 March–April. The measured γ-ray flux ($1.21 \pm 0.10 \times 10^{-5}$ ph cm^{-2} s^{-1} in a 0.1–300 GeV energy range) is the highest detected from 3C 279 by the *Fermi* Large Area Telescope. Hour-scale γ-ray flux variability is observed, with a flux doubling time as short as 1.19 ± 0.36 hr detected during one flare. The γ-ray spectrum is found to be curved at the peak of the flare, suggesting low probability of detecting very high energy (VHE; $E > 100$ GeV) emission, which is further confirmed by the VERITAS observations. The γ-ray flux increased by more than an order in comparison to a low-activity state and the flare consists of multiple sub-structures having a fast rise and slow decay profile. The flux enhancement is seen in all the wavebands, though at a lesser extent compared to γ-rays. During the flare, a considerable amount of the kinetic jet power gets converted to γ-rays and the jet becomes radiatively efficient. A one-zone leptonic emission model is used to reproduce the flare and we find increase in the bulk Lorentz factor as a major cause of the outburst. From the observed fast variability, lack of VHE detection, and the curved γ-ray spectrum, we conclude that the location of the emission region cannot be far out from the broad-line region (BLR) and contributions from both BLR and torus photons are required to explain the observed γ-ray spectrum.

Key words: galaxies: active – galaxies: jets – gamma rays: galaxies – quasars: individual (3C 279)

1. INTRODUCTION

Blazars are a peculiar class of active galactic nuclei (AGNs) with powerful relativistic jets aligned close to the line of sight to the observer (Urry & Padovani 1995). Because of the small inclination angle, the emission from their jet is relativistically amplified. The emitted radiation, predominantly by non-thermal emission processes, is highly luminous and shows rapid variations at all observed bands. Blazars are classified as flat spectrum radio quasars (FSRQs) and BL Lacertae (BL Lac) objects based on the rest-frame equivalent width (EW) of their broad optical emission lines, with FSRQs having EW >5 Å (Stickel et al. 1991; Stocke et al. 1991). However, Ghisellini et al. (2009) have proposed a new classification based on the broad-line region (BLR) luminosity in units of Eddington luminosity, with FSRQs having higher BLR luminosity ($L_{\rm BLR}/L_{\rm Edd} > 5 \times 10^{-4}$). Both classes share many common properties, such as flat radio spectra ($\alpha_r < 0.5$; $S_\nu \propto \nu^{-\alpha}$) at GHz frequencies, rapid flux, and polarization variations (Wagner & Witzel 1995; Andruchow et al. 2005), and exhibit superluminal patterns at radio wavelengths (Jorstad et al. 2005).

The broadband spectral energy distribution (SED) of blazars has two broad peaks, the first between millimeter and soft X-ray wavelengths, and the second in the MeV–GeV range. In general, FSRQs exhibit lower peak energies and higher bolometric luminosities than BL Lac objects (Fossati et al. 1998). Various models have been proposed to explain the broadband emission from blazars. The origin of the low-energy peak is understood to be associated with synchrotron radiation from relativistic electrons, whereas the high energy peak in the SED can be explained by the inverse-Compton (IC) scattering of synchrotron photons from the jet (synchrotron self-Compton (SSC); Konigl 1981; Marscher & Gear 1985; Ghisellini & Maraschi 1989). Alternatively, the seed photons for IC scattering can be external to the jet (external Compton (EC); Begelman & Sikora 1987; Melia & Konigl 1989; Dermer et al. 1992). A plausible reservoir of seed photons for EC can be the accretion disk (Dermer & Schlickeiser 1993; Böttcher et al. 1997), the BLR (Sikora et al. 1994; Ghisellini & Madau 1996), and the dusty torus (Błażejowski et al. 2000; Ghisellini & Tavecchio 2008). In contrast, the presence of the high energy peak has also been attributed to hadronic processes initiated by relativistic protons co-accelerated with the electrons (e.g., Mücke et al. 2003; Böttcher et al. 2013).

The quasar 3C 279 ($z = 0.536$; Lynds et al. 1965) is one of the first γ-ray-emitting blazars discovered by the Energetic Gamma-Ray Experiment Telescope on board the *Compton Gamma-Ray Observatory* (Hartman et al. 1992). This is also the first FSRQ detected in very high energy (VHE, $E >$ 100 GeV) γ-rays by the Major Atmospheric Gamma-ray Imaging Cherenkov (MAGIC) telescopes (MAGIC Collaboration et al. 2008), thus making it one of the farthest known VHE emitters to date (see also Mirzoyan 2014 for recent findings). It is strongly variable over the entire electromagnetic spectrum (e.g., Hayashida et al. 2012) with the γ-ray flux varying over two orders of magnitude, from $\sim 10^{-7}$ to $\sim 10^{-5}$ ph cm^{-2} s^{-1} above 100 MeV (Maraschi et al. 1994; Wehrle et al. 1998). An intense multi-wavelength monitoring of 3C 279 during a γ-ray flare in 2009 led to the discovery of the change in optical polarization in conjunction with the γ-ray flare (Abdo et al. 2010a). This source is bright in the hard X-ray band and is included in the 70 month *Swift* Burst Alert Telescope (BAT) catalog (Baumgartner et al. 2013). A multi-frequency study covering the first two years of the *Fermi Gamma-ray Space Telescope* mission has found the γ-rays to lead the optical emission by $\sim$10 days (Hayashida et al. 2012). The detection of an orphan X-ray flare with no clear counterpart in

other wavebands is also reported by them. Interestingly, there are observations of inconsistent patterns of correlation over various energy bands shown by 3C 279 (e.g., Chatterjee et al. 2008). At the radio wavelengths, 3C 279 exhibits a compact core and Very Long Baseline Array observations reveal superluminal patterns with apparent speed of (20.6 ± 0.8)c (Lister et al. 2013). Moreover, radio studies have also estimated the bulk Lorentz factor and viewing angle of the jet flow as $\Gamma_j = 15.5 \pm 2.5$ and $\Theta_j = 2\overset{\circ}{.}1 \pm 1\overset{\circ}{.}1$ (Jorstad et al. 2004, 2005).

Recently, 3C 279 was detected in an exceptionally high-activity state (Ciprini & Gonzalez 2014) by the Large Area Telescope (LAT) on board *Fermi* (hereafter *Fermi*-LAT; Atwood et al. 2009). We denote the period 2014 March 25 to 2014 April 13 (MJD 56,741–56,760) as a high-activity period. During this period, some of the brightest γ-ray flares since the beginning of the *Fermi*-LAT operation were observed from 3C 279. A special 350 ksec target of opportunity (ToO) observation was approved (between MJD 56,747–56,755) during which *Fermi*-LAT monitored this source in pointing mode, in addition to its normal survey mode operation. This flaring event was simultaneously monitored at low frequencies by the *Swift* satellite (Gehrels et al. 2004) and many ground-based observational facilities. In this work, motivated by the availability of near-simultaneous multi-wavelength data, we study this exceptional γ-ray outburst in detail. We also discuss the implications of our findings to constrain the location of the γ-ray emission region during the flare using a multi-wavelength approach. In Section 2, we report the details of the data reduction procedure and the results are presented in Section 3. We discuss our findings in Section 4 and conclude in Section 5. Throughout the work, we adopt a ΛCDM cosmology with the Hubble constant $H_0 = 71\,\mathrm{km\,s^{-1}\,Mpc^{-1}}$, $\Omega_m = 0.27$, and $\Omega_\Lambda = 0.73$.

2. MULTI-WAVELENGTH OBSERVATIONS AND DATA REDUCTION

2.1. Fermi-LAT Observations

The *Fermi*-LAT data used in this work were collected covering the period of the outburst (MJD 56,741–56,760) and a separate low-activity period (MJD 55,300–55,400). The standard data analysis procedure as mentioned in the *Fermi*-LAT documentation[4] is adopted. Events belonging to the energy range 0.1–300 GeV and SOURCE class are used. To select good time intervals (GTI), the filter "`DATA_QUAL>0`", & "`LAT_CONFIG==1`" is used and a cut of 100° is also applied on the zenith angle to avoid contamination from the Earth limb γ-rays. We consider the recently released galactic diffuse emission component gll_iem_v05_rev1.fits and an isotropic component iso_source_v05_rev1.txt as background models,[5] whose normalization parameters are left free to vary during the fitting. The unbinned likelihood method included in the pylikelihood library of `Science Tools (v9r33p0)` and the post-launch instrument response functions P7REP_SOURCE_V15 are used for the analysis. The significance of the γ-ray signal is computed by means of the maximum likelihood (ML) test statistic $\mathrm{TS} = 2\Delta \log(\mathcal{L})$ where $\mathcal{L}$ represents the likelihood function between models with and without a point source at the position of the source of interest. All the sources lying within a 10° region of interest (ROI) centered at the position of 3C 279 and defined in the second *Fermi*-LAT catalog (Nolan et al. 2012) are included in the analysis. All the parameters except the scaling factor of the sources within the ROI are allowed to vary during the likelihood fitting. Additionally, we also include the sources lying within 10° to 15° from the center of the ROI and keep their parameters fixed to the 2FGL catalog value. The γ-ray bright blazar 3C 273 lies at $\sim 10\overset{\circ}{.}3$ from 3C 279, and we keep its spectral parameters free during the fitting. We also search for the presence of unmodeled sources within the ROI by generating the residual TS maps for the periods covered in this work. We do not find any significant unmodeled source (i.e., source with $\mathrm{TS} > 25$). We perform a first run of the ML analysis over the period of interest and remove all the sources with $\mathrm{TS} < 25$. This updated model is then used for further temporal and spectral analysis. Though 3C 279 is modeled by a logParabola model in the 2FGL catalog, to generate light curves we use a power-law (PL) model as the PL indices obtained from this model show smaller statistical uncertainties when compared to those obtained from complex model fits. Moreover, since we want to probe the shortest timescales (hence lower photon statistics), adopting a simple PL model is appropriate. For the time series and spectral analysis, we consider the source to be detected if $\mathrm{TS} > 9$, which corresponds to $\sim 3\sigma$ detection (Mattox et al. 1996). Bins with $\mathrm{TS} < 9$ and/or $\Delta F_\gamma / F_\gamma > 0.5$, where ΔF_γ is the error estimate in the flux F_γ, are rejected from the analysis. Primarily governed by uncertainty in the effective area, the measured fluxes have energy-dependent systematic uncertainties of around 10% below 100 MeV, decreasing linearly in log(E) to 5% in the range between 316 MeV and 10 GeV and increasing linearly in log(E) up to 15% at 1 TeV.[6] All errors associated with the LAT data analysis are 1σ statistical uncertainties, unless specified.

2.2. Swift Observations

Throughout the flaring period, the *Swift* satellite has monitored 3C 279 almost regularly using all the three instruments on board it. However, due to the poor sensitivity of BAT (Barthelmy et al. 2005), it is not possible to extract the signal over the short time periods covered in this work. On the other hand, it is significantly detected by the X-ray Telescope (XRT; Burrows et al. 2005) as well as by the UltraViolet Optical Telescope (UVOT; Roming et al. 2005).

The XRT data are first processed with the XRTDAS software package (v.3.0.0) available within HEASOFT package (6.16). Event files are cleaned and calibrated using standard procedures (`xrtpipeline v.0.13.0`) with the calibration database updated on 2014 November 7. Standard grade selections of 0–12 in the photon counting mode are used. Energy spectrum is extracted from the summed event files. Since at the peak of the γ-ray flare, 3C 279 was extremely bright in the 0.3–10 keV band, we select annular regions centered at the source position to extract the source and the background spectra. This is required to avoid possible pile up effects. Inner and outer radii of the source region are chosen as $5''$ and $65''$ respectively, while the background spectra are extracted from an annular region of inner and outer radii of

[4] http://fermi.gsfc.nasa.gov/ssc/data/analysis/documentation/

[5] http://fermi.gsfc.nasa.gov/ssc/data/access/lat/BackgroundModels.html

[6] http://fermi.gsfc.nasa.gov/ssc/data/analysis/LAT_caveats.html

130″ and 230″, respectively. The selection of this particular choice of radii of annular regions is based on the task `xrtgrblc v.1.6 4`[7] (see also Stroh & Falcone 2013). Exposure maps are combined using XIMAGE and ancillary response files are generated using the task `xrtmkarf`. Source spectra are binned to have at least 20 counts per bin, using the task `grppha`. Spectral fitting is done using Xspec (Arnaud 1996). An absorbed PL ($N_H = 2.05 \times 10^{20}\,\mathrm{cm}^{-2}$; Kalberla et al. 2005) is used for fitting and the uncertainties are calculated at the 90% confidence level.

Swift/UVOT observations are integrated using `uvotimsum` and the parameters are extracted using the task `uvotsource`. Source region is selected as a circle centered at the source position and of 5″ radius, while background is chosen from a nearby source-free circular region with a radius of 1′. Observed magnitudes are corrected for galactic extinction following Schlafly & Finkbeiner (2011) and converted to flux units using the zero point magnitudes and conversion factors of Breeveld et al. (2011).

2.3. SMARTS Observations

A sample of γ-ray-emitting AGNs discovered by *Fermi*-LAT is being monitored by the Small and Moderate Aperture Research Telescope System (SMARTS) at the Cerro Tololo Inter-American Observatory located at Chile. Optical and near-infrared (IR) data from SMARTS are routinely available in *B, V, R, J*, and *K* bands. More details on data acquisition, reduction and calibration can be found in Bonning et al. (2012). For this work, we collected the publicly available data of 3C 279. The data in all the filters are corrected for galactic extinction following Schlafly & Finkbeiner (2011) and then converted to flux units using the zero points of Bessell et al. (1998).

2.4. Steward Observatory Monitoring

Optical photometric, spectrophotometric, and spectropolarimetric observations of *Fermi*-LAT detected blazars are being carried out at the Steward observatory at the University of Arizona as part of its monitoring program. Details of the data reduction and calibration procedures are presented in Smith et al. (2009). We downloaded the publicly available optical photometric and polarimetric data of 3C 279. The photometric V band observations are corrected for galactic reddening (Schlafly & Finkbeiner 2011) and converted to flux units following Bessell et al. (1998).

3. RESULTS

We select the period 2014 March 25–April 13 (MJD 56,741–56,760) for a detailed study of this brightest γ-ray flare observed from 3C 279 by *Fermi*-LAT. For comparison, we also select a γ-ray low-activity state, 2010 April 14–July 23 (MJD 55,300–55,400). These selected periods are shown with the symbols *F* and *Q*, representing flaring and low-activity state, respectively, in Figure 1, where we present the weekly binned γ-ray light curve of 3C 279 since the beginning of the *Fermi*-LAT operation.

[7] http://heasarc.gsfc.nasa.gov/lheasoft/ftools/headas/xrtgrblc.html

3.1. Multi-band Temporal Variability

In Figure 2, we show the multi-band light curves of 3C 279 from γ-rays to IR as well as optical polarization measurements, covering the period of high activity. In this plot, *Fermi*-LAT data points are one-day binned, whereas the observations in other wavebands are one point per observation Id. We divide the period of high activity into three sub-periods: Flare 1 (MJD 56,741–56,749), Flare 2 (MJD 56,749–56,755), and post-flare (MJD 56,755–56,760). These sub-periods are also selected taking into account the availability of near-simultaneous observations in other energy bands. From the low-cadence multi-band light curves in Figure 2, the flux variations at different wavelengths appear to be correlated. However, the presence or absence of time delays between different bands could not be statistically ascertained due to the fewer number of data points.

The multi-wavelength variability amplitudes of 3C 279 during the period of high activity are analyzed using the fractional rms variability amplitude parameter $F_{\rm var}$ (e.g., Vaughan et al. 2003). It is calculated as follows

$$F_{\rm var} = \frac{\left(S^2 - \Delta^2\right)^{1/2}}{\langle r \rangle} \tag{1}$$

where S^2 is the sample variance, $\langle r \rangle$ is the unweighted mean count rate, and Δ^2 is the mean square value of the uncertainties associated with each individual count rate. The error on $F_{\rm var}$ is computed following Vaughan et al. (2003):

$$\sigma_{F_{\rm var}} = \sqrt{\left(\sqrt{\frac{1}{2N}} \cdot \frac{\Delta^2}{\langle r \rangle^2 F_{\rm var}}\right)^2 + \left(\sqrt{\frac{\Delta^2}{N}} \cdot \frac{1}{\langle r \rangle}\right)^2} \tag{2}$$

where N is the number of data points. The maximum $F_{\rm var}$ is found for the γ-ray band and it decreases with frequency (see Table 1), a trend generally found in blazars (e.g., Zhang et al. 2005; Vercellone et al. 2010). The unusual high $F_{\rm var}$ for the K-band light curve could be due to the presence of two adjacent points where flux is varying abruptly (MJD 56,750 and 56,751). This is possibly due to bad weather conditions present during the observing run (SMARTS team 2015, private communication).

The good γ-ray photon statistics during this exceptional flaring event permit us to search for short timescale variability by using finer time bins. We generate 12, 6, and 3 hr binned γ-ray light curves covering the period of high activity and show them in Figure 3. In this figure, black data points correspond to the observations taken during the ToO monitoring. We scan this light curve to search for short time variability using the following equation:

$$F(t) = F(t_0) \cdot 2^{(t-t_0)/\tau} \tag{3}$$

where $F(t)$ and $F(t_0)$ are the fluxes at time t and t_0, respectively, and τ is the characteristic doubling/halving timescale. We also set the condition that the difference in flux at the epochs t and t_0 is at least significant at the 3σ level (Foschini et al. 2011). The results of this analysis are presented in Table 2. The shortest flux doubling time is found to be 1.19 ± 0.36 hr for the flare that occurred on MJD 56,746. Similar results have been reported by Brown (2013) for another bright blazar PKS 1510-089. Moreover, along with the

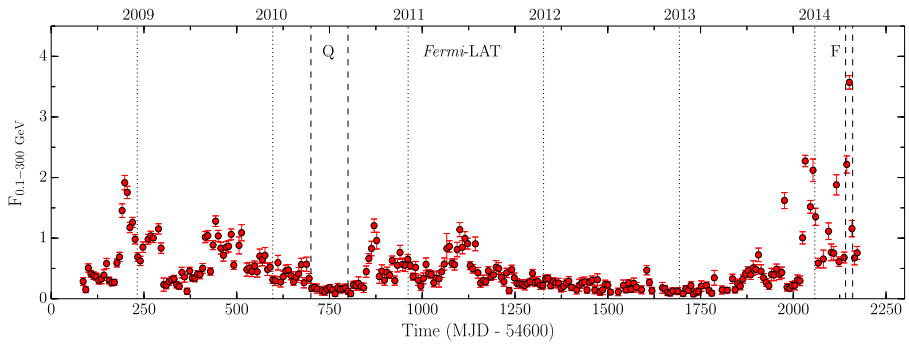

Figure 1. Weekly binned γ-ray light curve of 3C 279 with flux units of 10^{-6} ph cm^{-2} s^{-1}. A low-activity (Q) and flaring (F) periods are shown by dashed lines, whereas dotted lines represent the beginning of the new years.

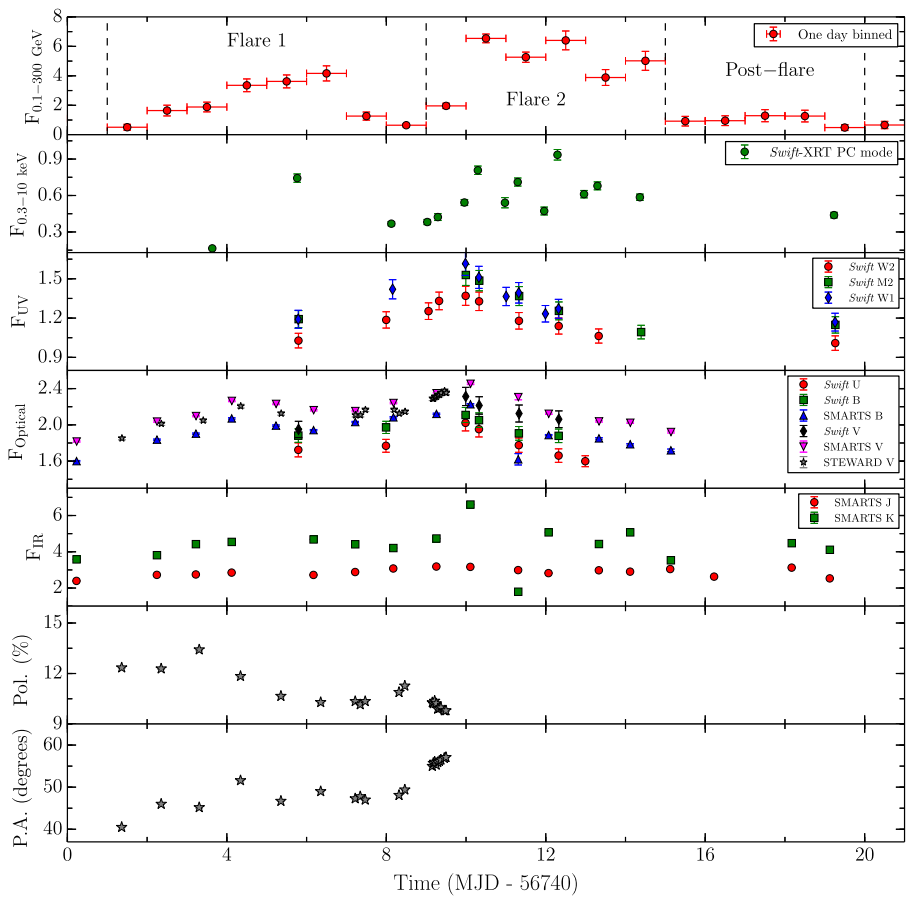

Figure 2. Multi-frequency light curve of 3C 279 covering the period of high activity. *Fermi*-LAT and *Swift*/XRT data points are in units of 10^{-6} ph cm^{-2} s^{-1} and counts s^{-1}, respectively. UV, optical, and IR fluxes have units of 10^{-11} erg cm^{-2} s^{-1}. See the text for details.

use of 3 hr binning, we also analyze the data using the time bins defined as GTI (Foschini et al. 2011). A GTI corresponds to the shortest time interval when the LAT data can be considered "valid".[8] The shortest flux doubling time using this method is obtained as 1.27 ± 0.36 hr on MJD 56,746, with $\sim 4\sigma$ significance. This is the first report of hour-scale γ-ray variability detected from 3C 279 since the launch of *Fermi*. The highest one-day averaged photon flux is found to be $(6.54 \pm 0.30) \times 10^{-6}$ ph cm^{-2} s^{-1} in the bin centered at MJD 56,750.5 and the corresponding photon index is 2.22 ± 0.04. Moreover, from the 3 hr binned γ-ray light curve, the peak flux and the associated photon index are found to be $(1.21 \pm 0.10) \times 10^{-5}$ ph cm^{-2} s^{-1} and 2.19 ± 0.09, respectively, again on the same day, i.e., MJD 56,750 (see Figure 3). This is the highest γ-ray flux measurement from 3C 279 since the beginning of *Fermi*-LAT mission.

The shortest 0.3–10 keV X-ray flux doubling time in the observed frame, estimated using Equation (3), is 8.11 ± 0.98 hr measured on MJD 56,752 with $\sim 9\sigma$ confidence. This coincides with a γ-ray flare (see Figure 3). The highest X-ray flux is found as $4.54^{+0.62}_{-0.49} \times 10^{-11}$ erg cm^{-2} s^{-1} measured on MJD 56,752. The obtained photon index is hard and has a value of $1.31^{+0.12}_{-0.13}$. This corresponds to an isotropic X-ray luminosity of 3.82×10^{46} erg s^{-1}.

[8] http://fermi.gsfc.nasa.gov/ssc/data/analysis/scitools/help/gtmktime.txt

Table 1
Fractional RMS Variability Amplitude ($F_{\rm var}$) Values for Different Energy Bands, Calculated for the Light Curves Shown in Figure 2

Energy Band	$F_{\rm var}$	Time Period	Number of Observations
K (SMARTS)	0.227 ± 0.001	56,742–56,760	15
J (SMARTS)	0.067 ± 0.002	56,742–56,760	16
V (Steward)	0.062 ± 0.002	56,741–56,749	20
V (SMARTS)	0.074 ± 0.001	56,742–56,760	16
V (UVOT)	0.083 ± 0.020	56,745–56,760	6
B (SMARTS)	0.089 ± 0.002	56,742–56,760	16
B (UVOT)	0.072 ± 0.016	56,745–56,760	7
U (UVOT)	0.081 ± 0.016	56,745–56,760	8
UVW1	0.097 ± 0.020	56,745–56,760	9
UVM2	0.119 ± 0.021	56,745–56,760	7
UVW2	0.096 ± 0.018	56,745–56,760	10
X-ray (0.3–10 keV)	0.347 ± 0.014	56,743–56,760	15
γ-ray (0.1–300 GeV)	0.739 ± 0.034	56,741–56,760	19

Note. Time periods during which observations were made. The total number of observations in that period are also given.

3.2. Highest Energy Gamma-ray Photon

To determine the energy of the highest energy photon detected from the source, we analyze the LAT data using the event class CLEAN. The tool `gtsrcprob` is used for this purpose. We find the highest energy photon of 13.54 GeV detected on 2014 April 3 (MJD 56,750.46209) at 2′.52 away from the position mentioned in the 2FGL catalog. The probability that the highest energy photon can be associated with the location, offset by 2′.52 from the position of 3C 279 mentioned in the 2FGL catalog, is 99.94%.

3.3. Gamma-ray Spectral Analysis

We generate the γ-ray spectra for all the four periods under consideration, namely Flare 1, Flare 2, post-flare, and a low-activity state. Analysis of the γ-ray spectral shape is done using two spectral models: PL ($dN/dE \propto E^{\Gamma_\gamma}$), where Γ_γ is the photon index and logParabola ($dN/dE \propto (E/E_{\rm o})^{-\alpha-\beta\, log\, (E/E_{\rm o})}$, where $E_{\rm o}$ is an arbitrary reference energy fixed at 300 MeV, α is the photon index at $E_{\rm o}$ and β is the curvature index that defines the curvature around the peak). To test for the presence of curvature, the test statistic of the curvature $\mathrm{TS_{curve}} = 2(\log \mathcal{L}$ (LogParabola) $-$ $\log \mathcal{L}$(PL)), is calculated. A $\mathrm{TS_{curve}}$ having a value greater than 16 suggests the presence of significant curvature in the γ-ray spectrum (Nolan et al. 2012). The resultant SEDs in the γ-ray band are shown in Figure 4 and the fitting parameters are given in Table 3. Significant curvature is noticed only during Flare 2 with $\mathrm{TS_{curve}} \approx 30$. Though at low significance, there is also a hint of the presence of curvature in the Flare 1 state ($\mathrm{TS_{curve}} \approx 8$).

3.4. Spectral Energy Distributions

3.4.1. Model Setup

We develop a simple one-zone leptonic emission model by following the procedures outlined in Ghisellini & Tavecchio (2009, hereafter GT09) and Dermer et al. (2009; see also Finke et al. 2008) to interpret the broadband emission from 3C 279. The emission region is assumed to be spherical, located at a distance of $R_{\rm diss}$ from the central black hole, and filled with electrons having a smooth broken PL energy distribution of

$$N'(\gamma') = N'_0 \frac{\left(\gamma'_b\right)^{-p}}{\left(\gamma'/\gamma'_b\right)^{p} + \left(\gamma'/\gamma'_b\right)^{q}}, \quad (4)$$

where p and q are the particle indices before and after the break energy (γ'_b), respectively (primed quantities are measured in the comoving frame). The emission region size is adopted by considering it to cover the entire jet cross-section with the jet semi-opening angle assumed to be 0.1 radian. The accretion disk is assumed to be of standard Shakura & Sunyaev (1973) type and producing a multi-temperature blackbody spectrum (Frank et al. 2002). It extends from $R_{\rm in,d} = 3R_{\rm Sch}$ to $R_{\rm out,d} = 500R_{\rm Sch}$, where $R_{\rm Sch}$ is the Schwarzschild radius. Above and below the accretion disk, the presence of an X-ray corona is also considered, which reprocesses a fraction $f_{\rm cor}$ of the accretion disk luminosity. The inner and outer radii of the corona are assumed to be $3R_{\rm Sch}$ and $30R_{\rm Sch}$, respectively. The spectrum of the X-ray corona is considered to be a cut-off PL: $L_{\rm cor}(\epsilon) \propto \epsilon^{-\alpha_{\rm cor}} \exp(-\epsilon/\epsilon_{\rm c})$ (GT09). The BLR is assumed to be a spherical shell located at a distance of $R_{\rm BLR} = 10^{17} L_{\rm d,45}^{1/2}$ cm, where $L_{\rm d,45}$ is the accretion disk luminosity in units of 10^{45} erg s^{-1}. It reprocesses a fraction $f_{\rm BLR}$ of the accretion disk luminosity. The SED of the BLR is approximated as an isotropic blackbody peaking at the rest-frame frequency of the Lyman-α line (Tavecchio & Ghisellini 2008). The dusty torus, for simplicity, is assumed to be a thin spherical shell located at a distance $R_{\rm torus} = 10^{18} L_{\rm d,45}^{1/2}$ cm, reprocessing a fraction $f_{\rm torus}$ of the accretion disk radiation in the IR. The spectrum of the torus is assumed as a blackbody with temperature $T_{\rm torus} = \epsilon_{\rm peak} m_{\rm e} c^2/3.93k$, where $\epsilon_{\rm peak}$ is the dimensionless peak photon energy and k is the Boltzmann constant. Following GT09, we calculate the relative contribution of these emissions with respect to the distance from the central black hole. Moreover, the synchrotron and SSC spectra are computed using the prescriptions of Finke et al. (2008). The external Compton emissions are calculated following GT09 (see also Dermer et al. 2009; Dermer & Menon 2009). Finally, the kinetic power of the jet is calculated by assuming protons to be cold, contributing only to the inertia of the jet, and having equal number density to that of the relativistic electrons (e.g., Celotti & Ghisellini 2008). To model the SEDs, we start with a plausible set of parameters that are then constrained by reproducing the observed fluxes at different energies.

3.4.2. SED Modeling Results

We generate the broadband SEDs of 3C 279 during a low-activity period and three sub-periods covering the flaring event. The fluxes over each of the four time intervals are averaged and the derived values are given in Table 4, except for *Fermi*-LAT data, which are presented in Table 3. The broadband SEDs are reproduced using the model presented in Section 3.4.1 and with the following assumptions: the spectral shape of the X-ray corona is assumed to be flat ($\alpha_{\rm cor} = 1$) and the high energy cut-off is fixed at 150 keV (GT09). Fractions of the accretion disk luminosity reprocessed by the X-ray corona, the BLR, and the dusty torus are adopted as 0.3, 0.1, and 0.5, respectively.

As discussed by Ghisellini et al. (2010), a powerful diagnostic to constrain the accretion disk luminosity and the black hole mass is through modeling of the accretion disk spectrum over the optical-UV part of the SED, provided the

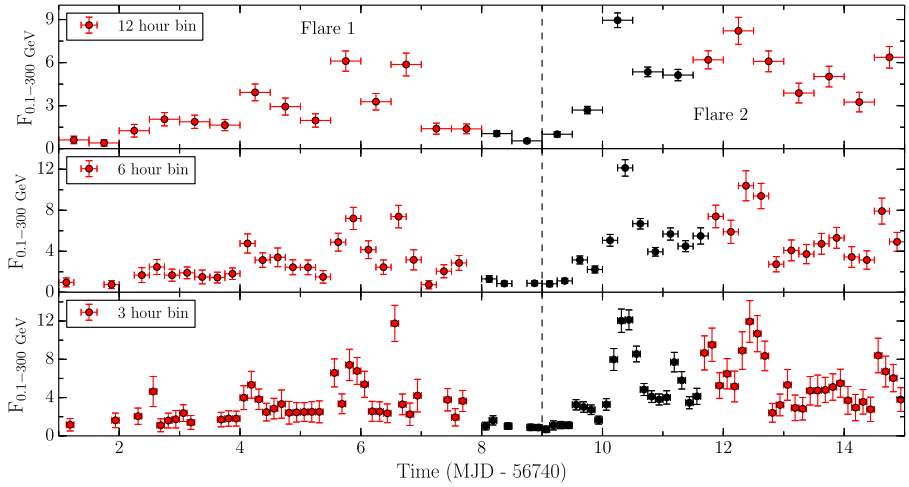

Figure 3. *Fermi*-LAT light curve of 3C 279 around the period of high activity, binned in intervals of 12, 6, and 3 hr (upper, middle, and lower panels, respectively). Black data points represent the *Fermi* ToO observations. The fluxes are in units of 10^{-6} ph cm^{-2} s^{-1}.

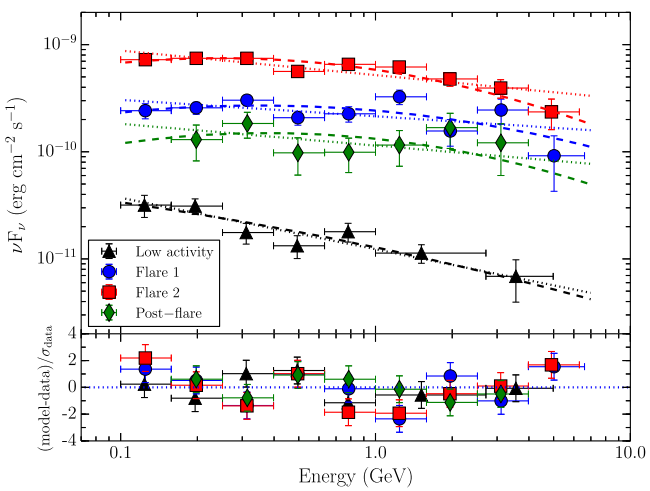

Figure 4. *Fermi*-LAT SEDs of 3C 279 during different activity states as defined in Table 3. Power-law and logParabola models are shown with dotted and dashed lines, respectively. Horizontal error bars correspond to the energy ranges of each bin, whereas vertical bars represent 1σ statistical errors. The residuals in the lower panel refer to the power-law model.

observed optical-UV spectrum is then reproduced by a combination of synchrotron and the accretion disk emissions. Accordingly, the derived accretion disk luminosity and the black hole mass are 1×10^{45} erg s^{-1} and 3×10^{8} $M_\odot$, respectively. These values are quite in agreement with that obtained in earlier studies (2×10^{45} erg s^{-1}, 3×10^{8} $M_\odot$; Pian et al. 1999; Woo & Urry 2002). Using the obtained accretion disk luminosity and the black hole mass, we model the SEDs covering the flaring period. The model spectra due to different emission mechanisms along with the observed fluxes are shown in Figure 5 and the relevant parameters are given in Table 5.

The size of the emission region is obtained as $R_{\rm blob} \sim 1 \times 10^{16}$ cm, constrained from the SED modeling. This corresponds to a variability time ($t_{\rm v} = R_{\rm blob}\ (1+z)/\delta c$; where the Doppler factor $\delta = 19$ taken from the SED modeling) of ~8 hr in the observers frame. The similarity of the variability time deduced from the SED modeling with that obtained using the shortest X-ray flux doubling timescale is striking. However, we find the shortest γ-ray flaring time to be as small as ~1 hr

Table 2
Summary of the Search for the Shortest Timescale of Variability Using 3 hr Binned γ-ray Light Curve

t	t_0	$F(t)$	$F(t_0)$	$\lvert\tau\rvert$	Signif.	R/D
56746.4376	56746.5626	1.91 ± 0.94	10.95 ± 1.92	1.19 ± 0.36	4.225	R
56746.5626	56746.6876	10.95 ± 1.92	2.94 ± 1.12	1.58 ± 0.51	3.599	D
56749.4376	56749.5626	1.03 ± 0.37	3.33 ± 0.57	1.78 ± 0.60	3.400	R
56750.0626	56750.1876	3.29 ± 0.65	7.57 ± 1.16	2.49 ± 0.75	3.219	R
56750.5626	56750.6876	8.34 ± 0.85	4.50 ± 6.26	3.37 ± 0.94	3.636	D

Note. Times t and t_0 are in MJD; fluxes are in units of 10^{-6} ph cm^{-2} s^{-1}; the absolute values of the observed characteristic timescale $\lvert\tau\rvert$ are in hours; the significance of the flux differences is in σ, and R and D denote the rise or decay time.

optical-UV bump (the big blue bump) is visible. Since the optical-UV spectrum of 3C 279 is dominated by non-thermal spectrum (e.g., Hayashida et al. 2012), we start with the modeling of the low-activity state where the probability of detecting thermal emission from the accretion disk is high. The optical-UV spectrum during the low-activity state shows a turnover at high energies (Figure 5), though it is not prominent. We attribute this excess to the accretion disk radiation. The

(Table 2). This hints at the existence of multiple γ-ray-emitting sub-structures within a larger emission region responsible for the flux enhancement in all the wavebands. These smaller regions could be responsible for the observed fast γ-ray variations. This is also supported from the observed 3 hr binned γ-ray light curve where many short time flaring events are seen (Figure 3). Since we generate the SEDs of the source by averaging the fluxes over larger time intervals, the results of the

Table 3
Results of the Model Fitting to the γ-ray Spectra of 3C 279, Obtained for Different Time Periods

Period [1]	Activity [2]	Model [3]	$F_{0.1\text{–}300\ \mathrm{GeV}}$ [4]	$\Gamma_{0.1\text{–}300\ \mathrm{GeV}/\alpha}$ [5]	β [6]	TS [7]	$\mathrm{TS_{curve}}$ [8]
55,300–55,400	Low activity	PL	0.16 ± 0.02	2.48 ± 0.08	⋯	315.61	⋯
	⋯	LP	0.15 ± 0.02	2.42 ± 0.13	0.04 ± 0.06	315.50	0.01
56,741–56,749	Flare 1	PL	1.64 ± 0.10	2.15 ± 0.05	⋯	1276.40	⋯
	⋯	LP	1.53 ± 0.10	1.96 ± 0.09	0.10 ± 0.04	1286.53	7.74
56,749–56,755	Flare 2	PL	4.47 ± 0.15	2.23 ± 0.03	⋯	4445.66	⋯
	⋯	LP	4.24 ± 0.15	2.05 ± 0.05	0.13 ± 0.03	4463.94	29.96
56,755–56,760	Post-flare	PL	0.95 ± 0.16	2.20 ± 0.11	⋯	204.39	⋯
	⋯	LP	0.83 ± 0.17	1.93 ± 0.23	0.13 ± 0.10	206.04	2.31

Note. Col.[1]: period of observation (MJD); Col.[2]: activity state; Col.[3]: model used (PL: power law, LP: logParabola); Col.[4]: integrated γ-ray flux (0.1–300 GeV), in units of 10^{-6} ph cm^{-2} s^{-1}; Col.[5] and [6]: spectral parameters (see definitions in the text); Col.[7]: test statistic; Col.[8]: $\mathrm{TS_{curve}}$.

Table 4
Summary of the SED Analysis

			Swift-XRT		
Activity State	Exp.[a]	$\Gamma_{0.3\text{-}10\ \mathrm{keV}}$[b]	$F_{0.3\text{-}10\ \mathrm{keV}}$[c]	Norm.[d]	Stat.[e]
Low activity	5.97	$1.62^{+0.06}_{-0.06}$	$1.01^{+0.06}_{-0.06}$	$1.36^{+0.07}_{-0.07}$	69.10/59
Flare 1	2.49	$1.53^{+0.08}_{-0.07}$	$2.01^{+0.15}_{-0.14}$	$2.48^{+0.15}_{-0.15}$	44.68/47
Flare 2	10.16	$1.47^{+0.03}_{-0.03}$	$2.54^{+0.09}_{-0.08}$	$2.93^{+0.08}_{-0.08}$	172.50/179
Post-flare	0.93	$1.77^{+0.15}_{-0.15}$	$1.01^{+0.20}_{-0.17}$	$2.35^{+0.25}_{-0.25}$	16.14/14

			Swift-UVOT			
Activity state	V[f]	B[f]	U[f]	UVW1[f]	UVM2[f]	UVW2[f]
Low activity	0.13 ± 0.01	0.11 ± 0.01	0.09 ± 0.01	0.10 ± 0.00	0.09 ± 0.00	0.09 ± 0.00
Flare 1	1.95 ± 0.09	1.93 ± 0.05	1.75 ± 0.05	1.31 ± 0.05	1.19 ± 0.07	1.11 ± 0.04
Flare 2	2.18 ± 0.05	1.99 ± 0.04	1.80 ± 0.03	1.40 ± 0.03	1.35 ± 0.03	1.24 ± 0.02
Post-flare	1.76 ± 0.09	1.62 ± 0.07	1.56 ± 0.07	1.17 ± 0.07	1.15 ± 0.06	1.01 ± 0.06

		SMARTS		
Activity state		R[g]	J[g]	K[g]
Low activity	⋯	0.16 ± 0.00	0.23 ± 0.00	0.49 ± 0.00
Flare 1	⋯	2.41 ± 0.00	2.84 ± 0.00	4.35 ± 0.00
Flare 2	⋯	2.49 ± 0.00	3.01 ± 0.01	4.62 ± 0.00
Post-flare	⋯	2.19 ± 0.01	2.83 ± 0.01	4.04 ± 0.01

Note. *Fermi*-LAT analysis results are given in Table 3.
[a] Net exposure in kiloseconds.
[b] Photon index of the absorbed power-law model.
[c] Observed flux in units of 10^{-11} erg cm^{-2} s^{-1}, in 0.3–10 keV energy band.
[d] Normalization at 1 keV in 10^{-3} ph cm^{-2} s^{-1} keV^{-1}.
[e] Statistical parameters: χ^2/dof.
[f] Average flux in *Swift V, B, U, W*1, *M*2, and *W*2 bands, in units of 10^{-11} erg cm^{-2} s^{-1}.
[g] Average flux in SMARTS *R, J,* and *K* bands, in units of 10^{-11} erg cm^{-2} s^{-1}.

SED modeling obtained are more likely the representation of the average characteristics of 3C 279 during the various activity states considered here.

4. DISCUSSION

The giant γ-ray outburst of 3C 279 in 2014 March–April together with the availability of near-simultaneous coverage at other wavelengths has made it possible to study this peculiar event in detail.

A recent study on the multi-wavelength behavior of 3C 279 (Hayashida et al. 2012) reported a significant correlation between optical and γ-rays for the period 2008–2010. However, they have not found a correlation between variations in X-ray and γ-ray bands. Another study of 3C 279 in 2011 by Aleksić et al. (2014) has led to the conclusion that X-ray and γ-ray flux variations are correlated whereas no significant correlation is seen between optical and γ-rays. Such inconsistent patterns of correlations are already seen in the long-term variability studies of 3C 279 (e.g., Chatterjee et al. 2008). For the flare under consideration in this work, visual inspection of the multi-frequency light curves (Figure 2) reveals the enhancement of the fluxes in all the wavebands. This suggests that a single emission region as well as the same electron population are responsible for the flaring emission. However, the generation of high temporal resolution γ-ray light curves during the flaring period reveals the presence of multiple shorter timescale flaring events. During the Flare 1 phase, two major flares are observed in a 12 hr binned light curve (one

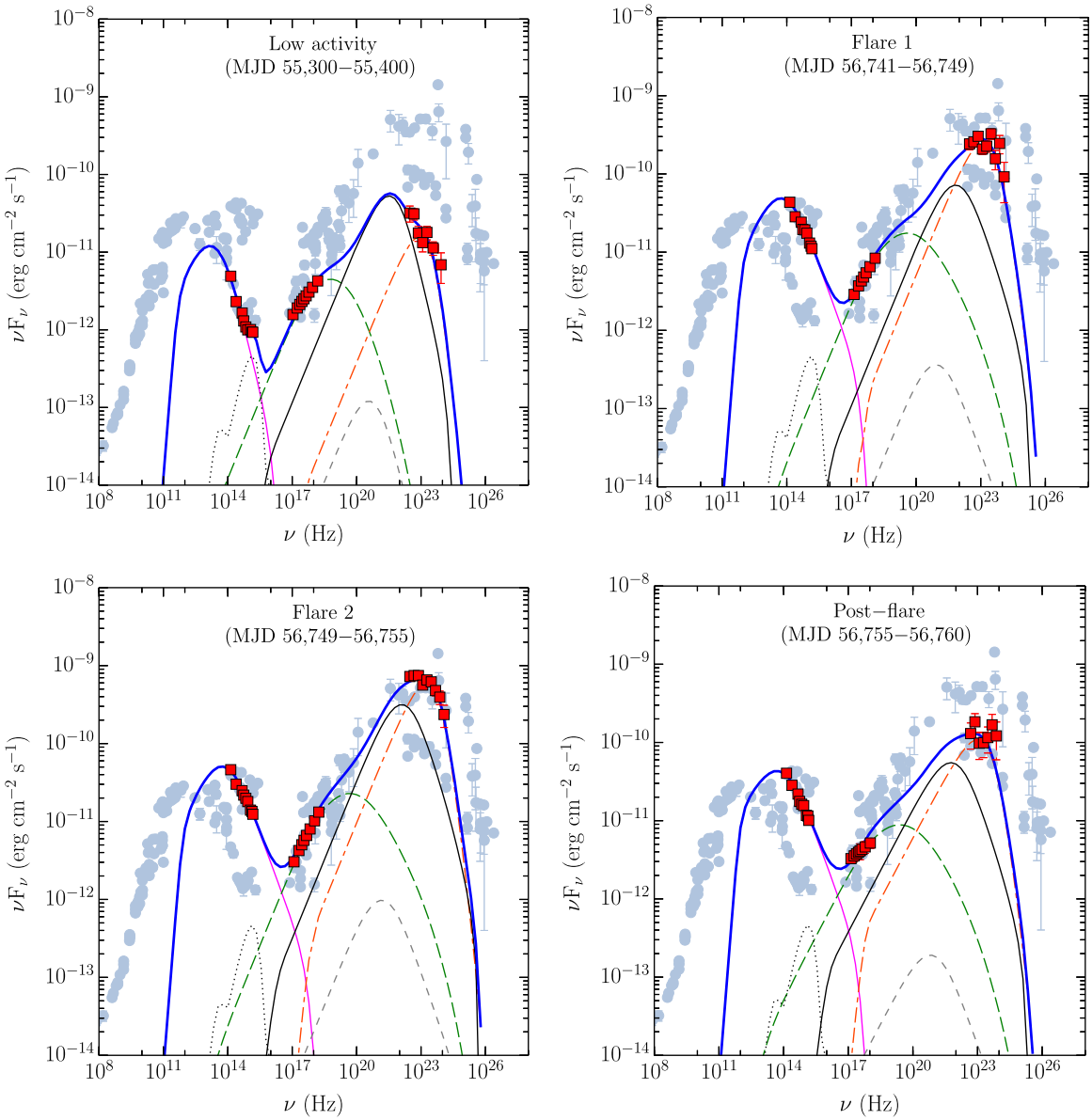

Figure 5. Spectral energy distributions of 3C 279 during low- and high-activity states. Simultaneous data from SMARTS, *Swift*, and *Fermi*-LAT are shown with red squares whereas light blue circles belongs to archival observations. The black dotted line represents thermal contributions from the torus, accretion disk, and X-ray corona (not in the plots). Pink thin solid and green dashed lines correspond to synchrotron and SSC emission, respectively. Gray dashed, red dash-dotted, and black dash-dot-dotted lines represent EC-disk, EC-BLR, and EC-torus components, respectively. The blue thick solid line is the sum of all the radiative mechanisms.

before MJD 56,746 and other after 12 hr). Interestingly, the former seems to be resolved in six- and three-hour bins, whereas the latter is non-resolvable down to three hours. Further, to understand the nature of the flares that occurred during the *Fermi* ToO observations (where the data have better signal-to-noise ratio than other periods), we use the following equation to fit the flare profiles (see, e.g., Abdo et al. 2010b)

$$F(t) = F_c + F_p\left(e^{\frac{t_p - t}{T_r}} + e^{\frac{t - t_p}{T_f}}\right)^{-1} \quad (5)$$

where F_c represents an assumed constant level underlying the flare, F_p measures the amplitude of the flare, t_p describes an approximate time of peak, and T_r and T_f are the rise and fall time, respectively. The results of the fitting of three flares (F1, F2, and F3) are shown in Figure 6 and the associated parameters are given in Table 6. Barring the third flare where we could not obtain the reliable parameters, the remaining two flares display a clear trend of fast rise and slow decay that can be interpreted as a result of particle acceleration mechanism. A fast rise of the flare could be attributed to the higher rate of acceleration, probably at a shock front, and the slow decay can be associated with the weakening of the shock.

From SED modeling, we find the location of the emission region at the outer edge of the BLR where the total energy density of the external soft photons are provided by the BLR clouds and the dusty torus in roughly equal fractions (see Figure 5). The primary mechanism for the production of γ-rays, thus, would be the IC scattering of BLR and torus photons. Accordingly, the cooling timescale for the electrons responsible for the emission of γ-rays ($\epsilon_\gamma = 1$ GeV), measured

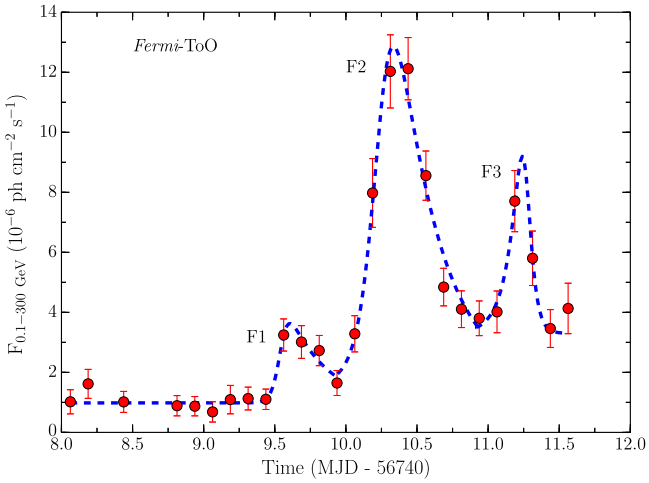

Figure 6. Three-hour binned γ-ray light curve of 3C 279 using the data taken in the pointed mode of the *Fermi*-LAT ToO observations. Only those bins when TS > 9 are used for fitting. F1, F2, and F3 correspond to the three flares for which fitting is performed. The dashed blue line represents the best-fit temporal profiles assuming an exponential rise and fall.

Table 5
Summary of the Parameters Used/Derived from the Modeling of the SEDs in Figure 5

Parameter	Low activity	Flare 1	Flare 2	Post-flare
p[a]	1.65	1.65	1.65	1.95
q[b]	5.2	4.5	4.5	4.5
B[c]	1.2	2.6	2.0	3.0
U_e'[d]	0.15	0.16	0.18	0.16
Γ[e]	10	13	19	14
γ_b'[f]	647	689	758	687
γ_{max}'[g]	1e4	3e4	5e4	3e4
R_{diss}[h]	0.045 (1570)	0.034 (1190)	0.035 (1220)	0.036 (1270)
P_e[i]	44.44	44.45	44.85	44.57
P_b[j]	44.00	44.68	44.80	44.92
P_r[k]	44.86	45.63	46.42	45.49
P_p[l]	46.48	46.48	46.86	46.97

Note. The viewing angle is taken as 3° and the characteristic temperature of the torus as 800 K. For a disk luminosity of 1×10^{45} erg s^{-1} and black hole mass of $3 \times 10^8\ M_\odot$, the size of the BLR is 0.03 parsec (1029 R_{Sch}).
[a] Slope of particle spectral index before break energy.
[b] Slope of particle spectral index after break energy.
[c] Magnetic field in Gauss.
[d] Particle energy density in erg cm^{-3}.
[e] Bulk Lorentz factor.
[f] Break Lorentz factor of electrons.
[g] Maximum Lorentz factor of electrons.
[h] Distance of the emission region from central black hole in parsecs (in R_{Sch}).
[i] Jet power in electrons in log scale.
[j] Magnetic jet power in log scale.
[k] Radiative jet power in log scale.
[l] Jet power in protons in log scale.

in the observers frame, would be (e.g., Saito et al. 2013)

$$\tau_{rad} \simeq \left(3m_e c/4\sigma_T u'_{total}\right) \times \left[\epsilon_0\left(1+z\right)/\epsilon_\gamma\right]^{0.5}, \quad (6)$$

i.e., ~7 minutes. Here, ϵ_0 is the characteristic energy of the seed photons (10.2 eV for BLR and 0.27 eV for torus photons) and u'_{total} is the total seed photon energy density in the comoving frame. The obtained cooling time is significantly shorter than the observed shortest flux halving time and the decay time of the flares (Tables 2 and 6). This suggests that the flare timescale is governed by the processes other than radiative losses, probably associated with particle acceleration or jet dynamics (Böttcher & Principe 2009; Kushwaha et al. 2014). Alternatively, the flare timescale can also be associated with the geometry and presence of sub-structures in the emitting region (see e.g., Tanihata et al. 2001).

The maximum γ-ray flux during the period of high activity is found to be $(1.21 \pm 0.10) \times 10^{-5}$ ph cm^{-2} s^{-1}, which corresponds to an isotropic γ-ray luminosity of 1.2×10^{49} erg s^{-1}. Adopting the bulk Lorentz factor $\Gamma = 19$ (obtained from the SED modeling of Flare 2), the total power emitted in the γ-ray band, in the proper frame of the jet, would be $L_{\gamma,em} \simeq L_\gamma/2\Gamma^2 \simeq 1.7 \times 10^{46}$ erg s^{-1}. This is a good fraction of the kinetic jet power (~23%; $P_{j,kin} = 7.2 \times 10^{46}$ erg s^{-1}). This implies that the jet becomes radiatively efficient and a significant amount of the kinetic jet power is released in the form of high-energy γ-ray radiation. Compared to the Eddington luminosity (L_{Edd}, for a black hole mass of $3 \times 10^8\ M_\odot$), $L_{\gamma,em}$ is about ~45% of L_{Edd}, thus supporting high radiative efficiency of the jet. Moreover, $L_{\gamma,em}$ is found to be 1.7 times larger than the total available accretion power ($L_{acc} \simeq L_{disk}/\eta_{disk} \simeq 1 \times 10^{46}$ erg s^{-1}; assuming radiative efficiency $\eta_{disk} = 10\%$). Recently, it has been established by Ghisellini et al. (2014) that, in blazars, the radiative jet power (to which the $L_{\gamma,em}$ is a good proxy) is of the same order of the accretion disk luminosity. The parameters obtained here, thus, indicate for the extremely efficient conversion of the accretion power and/or kinetic jet power to the jet γ-ray luminosity. Similar results have been found by Saito et al. (2013) for the GeV outburst of FSRQ PKS 1510-089. However, it should be noted that such events are short-lived only. This is due to the fact that the fraction of time in which the source is in a flaring state is about 1% (Tavecchio et al. 2010).

Comparing the SEDs corresponding to low- and flaring-activity states, we find that the flux has substantially increased across the electromagnetic spectrum. However, considering the SEDs during the three sub-phases of the flare, the major flux enhancement is observed in the γ-ray band, whereas a relatively lesser degree of flux variations is seen in the optical–UV and X-ray bands. This is also evident in the light curves shown in Figure 2. These changes are explained primarily by varying the bulk Lorentz factor, magnetic field, and particle energy density (Table 5). In addition to these, there are minor changes in other parameters such as the location of the emission region (and hence the emission region size), and spectral indices of the electron energy distributions. These changes are required to explain the variations in the X-ray spectra, in particular the post-flare X-ray spectrum, which is significantly softer than the other two sub-phases. These modifications, though minor, lead to large variations in the total jet power because γ_b' and p decide the total amount of electrons present in the emission region and thus the total number of cold protons (assuming both of them to have equal number densities). Interestingly, the maximum jet power is found during the post-flare rather than the peak of the γ-ray flux.

During Flare 2, a significant curvature in the γ-ray spectrum is noticed (see Figure 4 and Table 3). A similar feature is also noticed in the γ-ray spectrum of FSRQ 3C 454.3 during its

Table 6
Flare Characteristics Obtained by Fitting the Three Flares Seen during the *Fermi* ToO Monitoring (Figure 6).

Name	F_c	F_p	t_p	T_r	T_f	χ_r^2
F1	0.98 ± 0.13	3.73 ± 1.41	56749.55 ± 0.04	0.033 ± 0.026	0.268 ± 0.153	0.47
F2	1.61 ± 0.70	18.78 ± 2.56	56750.25 ± 0.04	0.078 ± 0.026	0.295 ± 0.062	1.71
F3	3.30 ± 0.24	10.93 ± 6.17	56751.26 ± 0.09	0.085 ± 0.042	0.038 ± 0.073	0.75

Note. Errors are estimated at the 1σ level. Fluxes F_c and F_p are in 10^{-6} ph cm^{-2} s^{-1}, t_p is in units of MJD, and T_r and T_f are in days.

giant outburst in 2010 November (Abdo et al. 2011). Poutanen & Stern (2010) have proposed a possible explanation of such curvature as being due to the attenuation of γ-rays by photon–photon pair production on He II Lyman recombination lines within the BLR. Recently, Cerruti et al. (2013) explained the origin of curved γ-ray spectrum as being due to the Klein–Nishina (KN) effect and a log-parabolic electron distribution. We reproduce the observed curvature in the γ-ray spectrum by the KN mechanism and with a broken PL electron distribution. In addition, we also adjust the BLR and torus energy densities in such a manner that the observed curvature can be explained by the superposition of these external photon fields (see a similar approach followed in Cerruti et al. 2013). Since in our model the radiation energy densities are a function of the distance from the central black hole, reproduction of the curvature in the γ-ray window of the SED can possibly hint at the location of the emission region. A similar approach is followed by Dermer et al. (2014) to explain the γ-ray spectra of 3C 279, though they also consider equipartition between various photon fields, particle energy density, and magnetic field. Interestingly, both studies (i.e., Cerruti et al. 2013; Dermer et al. 2014) concluded the location of the emission region to be at the outer edge of the BLR, akin to our findings. Moreover, a curvature in the γ-ray spectrum also suggests significant absorption of the VHE photons by the BLR radiation field (in the context of the above-mentioned discussion). Since we find a curvature during Flare 2, the probability of detecting VHE emission from 3C 279 during this period should be quite low. In fact, *Fermi*-LAT did not detect any VHE photon from 3C 279 during the entire flaring period (see Section 3.2). Additionally, preliminary results of the Very Energetic Radiation Imaging Telescope Array System (VERITAS) observations taken during Flare 2 also indicate the non-detection of VHE events from 3C 279 (Errando 2014).[9] The cut-off at GeV frequencies, as hinted by the curved LAT spectrum, upper limits in the VERITAS observations, and the measured short timescale variability, therefore suggests that the emission region cannot be far outside from the BLR.

The optical polarization monitoring from the Steward observatory indicates the anti-correlated behavior of the optical polarization with respect to the γ-ray flux (Figure 2). During the Flare 1 period, an enhancement in the γ-ray flux can be seen, but the optical polarization behaves opposite. At the same time, variation of the polarization angle follows a similar trend as seen in the γ-ray flux. Similar behavior from 3C 279 was earlier observed during its 2009 flare (Abdo et al. 2010a). Interestingly, though the γ-ray flux level during the recent outburst is much higher than that seen during the 2009 flare, the change in the optical polarization and polarization angle is relatively smaller. A possible reason could be that the γ-ray flare may be associated with the change in the optical polarization, not to a single coherent event but due to the superposition of multiple shorter duration events. In such a scenario, though the γ-ray flux increases, the overall polarization gets averaged out resulting in a lesser degree of change of polarization. This is supported by the short-duration flares seen in the three-hour binned γ-ray light curve. Moreover, as discussed below, we explain the flare due to bulk acceleration of the jet, which may not be directly related to the optical polarization, and hence, though there is significant change in the flux level, it is not reflected in the polarization observations. Unfortunately, we do not have polarimetric observations for the period of Flare 2 and thus it is not possible to predict the polarization behavior during the peak of the γ-ray activity.

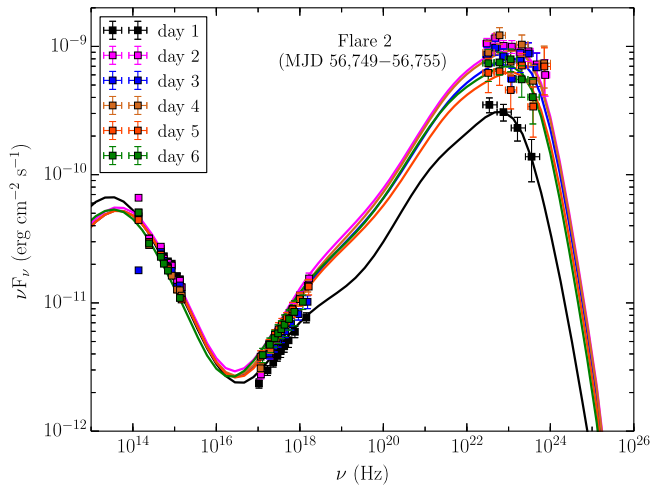

Figure 7. One day averaged SEDs of 3C 279 covering the main flaring period.

Swift and SMARTS have monitored 3C 279 almost every day during the Flare 2 period. This has enabled us to study the time evolution of the flare by generating the SEDs using finer time bins. In Figure 7, we show the one-day averaged SEDs covering the duration of Flare 2 and the corresponding modeling parameters are given in Table 7. In comparison to the optical and X-rays, a greater degree of enhancement in the γ-ray flux can be noticed. Since the optical and X-rays are due to synchrotron and SSC processes, respectively, and, γ-rays are due to EC mechanism, this difference could hint the possible change in the source parameters responsible for the flare. The synchrotron emissivity in the comoving frame can be approximated as (e.g., Shu 1991)

$$j'_{\rm syn}(\epsilon') \approx \frac{\sigma_{\rm T} c B^2}{48\pi^2} \epsilon_L^{-\frac{3}{2}} N'\left(\sqrt{\frac{\epsilon'}{\epsilon_L}}\right) \epsilon'^{\frac{1}{2}} \quad (7)$$

where $\epsilon_L = (h\nu_L/mc^2)$ is the quanta (dimensionless) corresponding to the Larmor frequency. On the other hand, the EC emissivity can be approximated as (Dermer 1995;

[9] http://files.aas.org/head14/106-11_Manel_Errando.pdf

Table 7
Summary of the Parameters Used/Derived from the Modeling of the SEDs in Figure 7

Parameter	Day 1	Day 2	Day 3	Day 4	Day 5	Day 6
p	1.5	1.7	1.7	1.7	1.7	1.7
q	4.4	4.5	4.5	4.5	4.5	4.5
B	4.6	2.5	2.5	2.5	2.5	2.7
U'_e	0.09	0.19	0.18	0.18	0.17	0.18
Γ	18	22	20	22	18	20
γ'_b	336	637	634	637	635	526
γ'_{max}	3e4	3e4	3e4	3e4	3e4	3e4
R_{diss}	0.034 (1170)	0.034 (1170)	0.034 (1170)	0.034 (1170)	0.034 (1180)	0.034 (1180)
P_e	44.45	44.97	44.85	44.95	44.76	44.87
P_b	45.44	45.08	45.00	45.09	44.92	45.08
P_r	45.97	46.79	46.52	46.77	46.26	46.47
P_p	46.43	47.07	46.96	47.05	46.86	47.00

Note. Symbols have the same meanings as in Table 5.

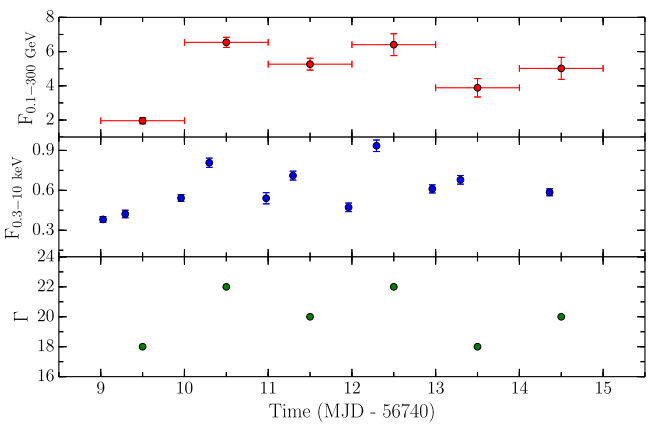

Figure 8. Variation of bulk Lorentz factor Γ as a function of time (bottom panel). For comparison, the variation of X-ray and γ-ray fluxes are also shown (top two panels). Units are the same as in Figure 2. Horizontal error bars represent the time ranges.

Sahayanathan & Godambe 2012)

$$j'_{ec}(\epsilon') \approx \frac{c\sigma_T u^\star}{8\pi\epsilon^\star}\left(\frac{\Gamma\epsilon'}{\epsilon^\star}\right)^{\frac{1}{2}} N'\left[\left(\frac{\epsilon'}{\Gamma\epsilon^\star}\right)^{\frac{1}{2}}\right] \quad (8)$$

where starred quantities are in the AGN frame. Comparing Equations (7) and (8) we find that the excess in EC emissivity can be obtained by increasing the jet bulk Lorentz factor without altering the synchrotron emissivity. An increase in Γ will also result in further boosting of the observed synchrotron, SSC, and EC fluxes in addition to the increase in emissivity of the EC. To illustrate this, in Figure 8 we show the variation of Γ, obtained from the SED modeling, along with the variation of X-ray and γ-ray fluxes. Clearly, the pattern of variability seen in X-rays and γ-rays is similar to that obtained in Γ.

Recently, Aleksić et al. (2014) have reported the multi-wavelength study of 3C 279 covering a low- and a high-activity period in 2011. In both activity states, the source was monitored by MAGIC telescopes. They could not ascertain the location of the emission region in the low-activity state because the SED and the relevant modeling parameters are found to be satisfactorily explained by both inside the BLR and outside the BLR scenario. However, the absence of the simultaneous data points covering NIR to UV frequencies hampers their interpretation (see their Figure 8). This is because the slope of the high-energy synchrotron spectrum constrains the shape of the falling IC spectrum, which lies in the LAT energy range (assuming that the same electron population is responsible for the emission at both regimes). The lack of the optical-UV data points, thus, could lead to the degeneracy in reproducing the SEDs. In contrast, the availability of the contemporaneous data from NIR to UV in the low-activity state SED modeled by us not only constrains the slope of the falling synchrotron spectrum but also the accretion disk radiation. It can be seen in the low-activity state SED in Figure 5 that either the EC-BLR or EC-torus alone cannot explain the observed γ-ray spectrum and hence a combination of both is required. This constrains the location of the emission region as, in our model, the radiation energy densities are a function of dissipation distance from the central black hole. Further, Aleksić et al. (2014) have fitted the SED of a high-activity state of 3C 279 with a two-zone leptonic model. This choice was driven by the observed correlated X-ray and γ-ray variations as well as by the lack of correlations seen between the optical and other wavebands. In this two-zone model, the X-ray to γ-ray emitting region lies inside the BLR (so as to explain the LAT spectrum and MAGIC upper limits), whereas the low-energy emitting region lies outside the BLR. During the high-activity state studied in our work, we find enhancement in fluxes at all the wavelengths, which, unlike the 2011 flare, supports the single-zone origin of the radiations. However, similar to them, the shape of the LAT spectrum and non-detection by VERITAS suggest that the BLR has a significant impact on the observed γ-ray spectrum and thus the emission region cannot be far out from it.

Hayashida et al. (2012) studied 3C 279 using an extensive broadband data set covering the first two years of the *Fermi* operation. They report the presence of double synchrotron peaks at mid- to far-IR frequencies and a delay of about 10 days between the optical and γ-rays as found from cross-correlation studies. Interestingly, they argue that X-rays do not correlate with optical and γ-ray fluxes during the flaring states and hence X-ray data are not accounted for their SED modeling. In comparison to that, we find similar behavior of the fluxes at different wavelengths. In the modeling performed by the Hayashida et al. (2012), the location of the emission region is constrained on the basis of the observed change of the optical polarization and the associated rotation of the electric vector polarization angle (EVPA), which was accompanied by the γ-ray flare (see also Abdo et al. 2010a). Though the flux amplitude is much higher during the 2014 γ-ray flare, the corresponding rotation of the EVPA as well as change in the optical polarization are found to be much less than that obtained during the 2009 flare. However, we stress that we do not have polarization data during the main flaring event and thus a strong claim regarding the variability of optical polarization associated with the γ-ray flaring event cannot be made. There are few other differences such as their use of a comparatively long variability timescale ($\approx$2 weeks) and a double broken PL electron energy distribution. Their modeled magnetic field is also relatively lower compared to the one obtained by us.

In the model by Sahayanathan & Godambe (2012), where the authors discuss the 2006 flare of 3C 279, the emission region is assumed to be far out from the BLR, to avoid severe attenuation of VHE γ-rays by the BLR Lyman-α line emission. Their model overpredicts the γ-ray flux at MeV energies by about an order higher than that ever observed from 3C 279. Since there are no MeV–GeV observations available at the time of flare, this possibility cannot be ruled out. However, as discussed by Dermer et al. (2014), fitting the VHE data (along with the LAT spectrum) with single-zone leptonic emission models will result in the parameters being well out of equipartition. Alternatives to avoid such issues could be the use of multi-zone emission modeling or the inclusion of the hadronic radiation scenario (see, e.g., Böttcher et al. 2009). Since during the 2014 flare there is no detection of VHE events and the γ-ray spectrum is curved, the parameters obtained by us (under near-equipartition condition) using a single-zone leptonic emission model seems to be robust.

5. SUMMARY

In this paper, a detailed study of the brightest γ-ray flare observed from 3C 279 in 2014 March–April is presented. Below we summarize our main findings.

1. In the energy range of 0.1–300 GeV, the maximum γ-ray flux of $(1.21 \pm 0.10)\times10^{-5}$ ph cm^{-2} s^{-1} is observed on MJD 56,750. This is the highest γ-ray flux detected from 3C 279 since the launch of the *Fermi* satellite.
2. The shortest γ-ray flux doubling time measured is 1.19 ± 0.36 hr on MJD 56,746.
3. A significant curvature is noticed in the γ-ray spectrum during Flare 2. This suggests the low probability of detecting VHE events and is confirmed by the non-detection by VERITAS.
4. During the flare, the jet becomes radiatively efficient and a good fraction of kinetic power gets converted to high-energy γ-ray radiation.
5. During the Flare 1 phase, variation in the optical polarization and the rotation of EVPA are smaller compared to 2009 flare. However, we do not have a polarization measurement during Flare 2 and thus predicting the polarization behavior during the peak of the γ-ray emission is not possible.
6. A simple one-zone leptonic emission model satisfactorily explains the observed SEDs with an increase in the bulk Lorentz factor as a major cause of the flare.
7. Observations such as the presence of a significant curvature in the γ-ray spectrum, short timescale of variability, and the lack of VHE γ-rays suggest the location of the emission region to be at the outer edge of the BLR where both BLR and torus energy densities are contributing to the observed γ-ray spectrum.

We thank the referee for a constructive report that helped to improve the manuscript. V.S.P. is grateful to Gang Cao for useful discussions and suggestions. This research has made use of data, software, and/or web tools obtained from NASA's High Energy Astrophysics Science Archive Research Center (HEASARC), a service of Goddard Space Flight Center and the Smithsonian Astrophysical Observatory. Part of this work is based on archival data, software, or online services provided by the ASI Science Data Center (ASDC). This research has made use of the XRT Data Analysis Software (XRTDAS) developed under the responsibility of the ASDC, Italy. Data from the Steward Observatory spectropolarimetric monitoring project were used. This program is supported by *Fermi* Guest Investigator grants NNX08AW56G, NNX09AU10G, and NNX12AO93G. This paper has made use of up-to-date SMARTS optical/near-infrared light curves that are available at www.astro.yale.edu/smarts/glast/home.php. Use of the *Hydra* cluster at the Indian Institute of Astrophysics is acknowledged.

Facilities: CTIO: 1.3m, *Fermi*, *Swift*.

REFERENCES

Abdo, A. A., Ackermann, M., Ajello, M., et al. 2010a, Natur, 463, 919
Abdo, A. A., Ackermann, M., Ajello, M., et al. 2010b, ApJ, 722, 520
Abdo, A. A., Ackermann, M., Ajello, M., et al. 2011, ApJL, 733, L26
Aleksić, J., Ansoldi, S., Antonelli, L. A., et al. 2014, A&A, 567, A41
Andruchow, I., Romero, G. E., & Cellone, S. A. 2005, A&A, 442, 97
Arnaud, K. A. 1996, in ASP Conf. Ser. Vol. 101, Astronomical Data Analysis Software and Systems V, ed. G. H. Jacoby, & J. Barnes (San Francisco, CA: ASP), 17
Atwood, W. B., Abdo, A. A., Ackermann, M., et al. 2009, ApJ, 697, 1071
Barthelmy, S. D., Barbier, L. M., Cummings, J. R., et al. 2005, SSRv, 120, 143
Baumgartner, W. H., Tueller, J., Markwardt, C. B., et al. 2013, ApJS, 207, 19
Begelman, M. C., & Sikora, M. 1987, ApJ, 322, 650
Bessell, M. S., Castelli, F., & Plez, B. 1998, A&A, 333, 231
Błażejowski, M., Sikora, M., Moderski, R., & Madejski, G. M. 2000, ApJ, 545, 107
Bonning, E., Urry, C. M., Bailyn, C., et al. 2012, ApJ, 756, 13
Böttcher, M., Mause, H., & Schlickeiser, R. 1997, A&A, 324, 395
Böttcher, M., & Principe, D. 2009, ApJ, 692, 1374
Böttcher, M., Reimer, A., & Marscher, A. P. 2009, ApJ, 703, 1168
Böttcher, M., Reimer, A., Sweeney, K., & Prakash, A. 2013, ApJ, 768, 54
Breeveld, A. A., Landsman, W., Holland, S. T., et al. 2011, in AIP Conf. Proc. 1358, Gamma-Ray Burst 2010, ed. J. E. McEnery, J. L. Racusin, & N. Gehrels (Melville, NY: AIP), 373
Brown, A. M. 2013, MNRAS, 431, 824
Burrows, D. N., Hill, J. E., Nousek, J. A., et al. 2005, SSRv, 120, 165
Celotti, A., & Ghisellini, G. 2008, MNRAS, 385, 283
Cerruti, M., Dermer, C. D., Lott, B., Boisson, C., & Zech, A. 2013, ApJL, 771, L4
Chatterjee, R., Jorstad, S. G., Marscher, A. P., et al. 2008, ApJ, 689, 79
Ciprini, S., & Gonzalez, J. B. 2014, ATel, 6036, 1
Dermer, C. D. 1995, ApJL, 446, L63
Dermer, C. D., Cerruti, M., Lott, B., Boisson, C., & Zech, A. 2014, ApJ, 782, 82
Dermer, C. D., Finke, J. D., Krug, H., & Böttcher, M. 2009, ApJ, 692, 32
Dermer, C. D., & Menon, G. 2009, High Energy Radiation from Black Holes: Gamma Rays, Cosmic Rays, and Neutrinos (Princeton, NJ: Princeton Univ. Press)
Dermer, C. D., & Schlickeiser, R. 1993, ApJ, 416, 458
Dermer, C. D., Schlickeiser, R., & Mastichiadis, A. 1992, A&A, 256, L27
Errando, M. 2014, AAS/High Energy Astrophysics Division, 14, 106.11
Finke, J. D., Dermer, C. D., & Böttcher, M. 2008, ApJ, 686, 181
Foschini, L., Ghisellini, G., Tavecchio, F., Bonnoli, G., & Stamerra, A. 2011, A&A, 530, A77
Fossati, G., Maraschi, L., Celotti, A., Comastri, A., & Ghisellini, G. 1998, MNRAS, 299, 433
Frank, J., King, A., & Raine, D. J. 2002, Accretion Power in Astrophysics (3rd ed.; Cambridge: Univ. Cambridge Press)
Gehrels, N., Chincarini, G., Giommi, P., et al. 2004, ApJ, 611, 1005
Ghisellini, G., & Madau, P. 1996, MNRAS, 280, 67
Ghisellini, G., & Maraschi, L. 1989, ApJ, 340, 181
Ghisellini, G., Maraschi, L., & Tavecchio, F. 2009, MNRAS, 396, L105
Ghisellini, G., & Tavecchio, F. 2008, MNRAS, 387, 1669
Ghisellini, G., & Tavecchio, F. 2009, MNRAS, 397, 985
Ghisellini, G., Tavecchio, F., Foschini, L., et al. 2010, MNRAS, 402, 497
Ghisellini, G., Tavecchio, F., Maraschi, L., Celotti, A., & Sbarrato, T. 2014, Natur, 515, 376
Hartman, R. C., Bertsch, D. L., Fichtel, C. E., et al. 1992, ApJL, 385, L1
Hayashida, M., Madejski, G. M., Nalewajko, K., et al. 2012, ApJ, 754, 114
Jorstad, S. G., Marscher, A. P., Lister, M. L., et al. 2004, AJ, 127, 3115
Jorstad, S. G., Marscher, A. P., Lister, M. L., et al. 2005, AJ, 130, 1418

Kalberla, P. M. W., Burton, W. B., Hartmann, D., et al. 2005, A&A, 440, 775
Konigl, A. 1981, ApJ, 243, 700
Kushwaha, P., Sahayanathan, S., Lekshmi, R., et al. 2014, MNRAS, 442, 131
Lister, M. L., Aller, M. F., Aller, H. D., et al. 2013, AJ, 146, 120
Lynds, C. R., Stockton, A. N., & Livingston, W. C. 1965, ApJ, 142, 1667
MAGIC Collaboration, Albert, J., Aliu, E., et al. 2008, Sci, 320, 1752
Maraschi, L., Grandi, P., Urry, C. M., et al. 1994, ApJL, 435, L91
Marscher, A. P., & Gear, W. K. 1985, ApJ, 298, 114
Mattox, J. R., Bertsch, D. L., Chiang, J., et al. 1996, ApJ, 461, 396
Melia, F., & Konigl, A. 1989, ApJ, 340, 162
Mirzoyan, R. 2014, ATel, 6349, 1
Mücke, A., Protheroe, R. J., Engel, R., Rachen, J. P., & Stanev, T. 2003, APh, 18, 593
Nolan, P. L., Abdo, A. A., Ackermann, M., et al. 2012, ApJS, 199, 31
Pian, E., Urry, C. M., Maraschi, L., et al. 1999, ApJ, 521, 112
Poutanen, J., & Stern, B. 2010, ApJL, 717, L118
Roming, P. W. A., Kennedy, T. E., Mason, K. O., et al. 2005, SSRv, 120, 95
Sahayanathan, S., & Godambe, S. 2012, MNRAS, 419, 1660
Saito, S., Stawarz, Ł., Tanaka, Y. T., et al. 2013, ApJL, 766, L11
Schlafly, E. F., & Finkbeiner, D. P. 2011, ApJ, 737, 103
Shakura, N. I., & Sunyaev, R. A. 1973, A&A, 24, 337
Shu, F. H. 1991, Radiation: The Physics of Astrophysics (Vol. 1; Mill Valley, CA: Univ. Science Books)
Sikora, M., Begelman, M. C., & Rees, M. J. 1994, ApJ, 421, 153
Smith, P. S., Montiel, E., Rightley, S., et al. 2009, arXiv:0912.3621
Stickel, M., Padovani, P., Urry, C. M., Fried, J. W., & Kuehr, H. 1991, ApJ, 374, 431
Stocke, J. T., Morris, S. L., Gioia, I. M., et al. 1991, ApJS, 76, 813
Stroh, M. C., & Falcone, A. D. 2013, ApJS, 207, 28
Tanihata, C., Urry, C. M., Takahashi, T., et al. 2001, ApJ, 563, 569
Tavecchio, F., & Ghisellini, G. 2008, MNRAS, 386, 945
Tavecchio, F., Ghisellini, G., Bonnoli, G., & Ghirlanda, G. 2010, MNRAS, 405, L94
Urry, C. M., & Padovani, P. 1995, PASP, 107, 803
Vaughan, S., Edelson, R., Warwick, R. S., & Uttley, P. 2003, MNRAS, 345, 1271
Vercellone, S., D'Ammando, F., Vittorini, V., et al. 2010, ApJ, 712, 405
Wagner, S. J., & Witzel, A. 1995, ARA&A, 33, 163
Wehrle, A. E., Pian, E., Urry, C. M., et al. 1998, ApJ, 497, 178
Woo, J.-H., & Urry, C. M. 2002, ApJ, 579, 530
Zhang, Y. H., Treves, A., Celotti, A., Qin, Y. P., & Bai, J. M. 2005, ApJ, 629, 686